Frontal Dynamics near and following Frontal Collapse

CHRIS SNYDER, WILLIAM C. SKAMAROCK, AND RICHARD ROTUNNO

National Center for Atmospheric Research, * *Boulder, Colorado*

(Manuscript received 12 October 1992, in final form 22 March 1993)

ABSTRACT

A nonhydrostatic numerical model is used to simulate two-dimensional frontogenesis forced by either horizontal deformation or shear. Both inviscid frontogenesis prior to frontal collapse and frontogenesis with horizontal diffusion following collapse are considered. The numerical solutions generally agree well with semigeostrophic (SG) theory, though differences can be substantial for intense fronts. Certain deviations from SG that have been previously discussed in the literature are, upon closer examination, associated with spurious gravity waves produced by inadequate resolution or by the initialization of the numerical model. Even when spurious waves are eliminated, however, significant deviations from SG still exist: gravity waves are emitted by the frontogenesis when the cross-front scale becomes sufficiently small, and higher-order corrections to SG may also be present. In the postcollapse solutions (where they are most prominent), the emitted waves are stationary with respect to the front and lead to a band of increased low-level ascent just ahead of the surface front. It is suggested here that, when small, the deviations from SG arise as the linear forced response to the cross-front accelerations neglected by SG.

1. Introduction

Building on the early diagnostic studies of Sawyer (1956) and Eliassen (1962), the semigeostrophic (SG) theory of Hoskins and Bretherton (1972) has explained the basic dynamics of frontogenesis (for a somewhat different perspective, see also Williams 1972). Semigeostrophic theory predicts the formation of a frontal singularity in a finite time, a prediction that has been supported numerically, within the limits of their discretization, by primitive equation (PE) models (Gall et al. 1987; Garner 1989). As the frontal scale becomes increasingly small, however, the cross-front geostrophic balance assumed by SG becomes increasingly poor (Hoskins and Bretherton 1972; Davies and Müller 1988), and there is the likelihood that dynamical effects ignored by SG will then be important. In this paper, we use a nonhydrostatic numerical model to examine idealized, two-dimensional fronts prior to and following the time of frontal collapse predicted by SG. Our principal concern is the behavior of fronts in regimes where SG solutions are potentially incomplete or invalid; in such regimes, an important associated issue is the extent to which frontal dynamics remain balanced or, conversely, the extent to which frontogenesis emits gravity waves. With horizontal grid spacing of $O(10$ km$)$, we

Corresponding author address: Dr. Chris Snyder, NCAR, P.O. Box 3000, Boulder, CO 80307-3000.

find only small differences between PE and SG dynamics for inviscid, precollapse solutions, as long as spurious gravity wave sources are excluded from the simulations. At times beyond SG frontal collapse, however, emitted gravity waves of significant amplitude appear in the cross-front circulation from solutions with horizontal diffusion.

Although there have been previous PE simulations of two-dimensional fronts, their results concerning the latter stages of frontal development differ in important aspects. Gall et al. (1988, hereafter GWC) used a nonhydrostatic model to simulate inviscid, deformation-induced frontogenesis. In these high-resolution solutions (with horizontal and vertical grid spacings of less than 5 km and 320 m, respectively), a train of gravity waves, stationary with respect to the front, eventually appears above the frontal surface. These results, however, are at odds with Garner's (1989, hereafter G89) simulations of frontal collapse using a Lagrangian numerical model. Garner's solutions exhibit no noticeable counterpart of the GWC waves, but do possess a distinctive split in the frontal updraft near the "nose" of the front, as well as disturbances that propagate away from the front (counterparts of which were also noted by GWC). None of the above features are found in SG solutions, whose vertical velocity is smooth and has a single maximum right up to the time of collapse. Since the simulations of both GWC and G89 include no explicit dissipation, there is a tendency for the solutions to become poorly resolved as the frontogenesis proceeds, and numerical errors in one or both models might thus reasonably explain these discrepancies. In-

deed, inadequate resolution of sloping baroclinic zones in gridpoint models is known to produce spurious gravity waves (Pecnick and Keyser 1989; Persson and Warner 1991).

In contrast to GWC and G89, other numerical studies, which looked at times farther from SG frontal collapse or used substantial horizontal diffusion, have agreed well with SG predictions. Koclas et al. (1986), whose integrations stopped 5 hours before the time of collapse predicted by SG, found that their finite-element PE simulations of the deformation-induced front were very similar to analytic SG solutions. Reeder and Keyser (1988) reached similar conclusions for frontogenesis forced by a combination of confluence and horizontal shear, although they noted that significant local differences between their PE and SG solutions could appear near intense upper-level fronts.

A further question is whether the SG prediction of a frontal singularity holds for the PE. Orlanski and Ross (1984) proposed that the terms neglected by SG could restrict frontal collapse by shifting the horizontal convergence relative to the vertical vorticity, but other simulations have found this mechanism to be ineffective (Gall et al. 1987; Reeder and Keyser 1988; G89). In particular, both Gall et al. (1987) and G89 employ specialized numerical techniques to achieve high horizontal resolution near the front, and both find that the frontal scale becomes as small as the numerical discretization will allow. Garner also shows that SG accurately predicts the time and location of frontal collapse. Although this problem will not concern us here, neither of these studies proves that an inviscid "brake" for frontogenesis may not exist once the front collapses to sufficiently small scales, since even the Lagrangian simulations of G89 contain potentially large truncation errors near the front (see section 3b of G89). Nevertheless, such results do imply that, as a practical matter, numerically simulated inviscid fronts will collapse to the grid scale in models with horizontal resolutions of O(1 km).

Few theoretical treatments of frontal dynamics near collapse exist and, relatedly, there has been little agreement on the interpretation of PE frontal simulations. Ley and Peltier (1978) examined the emission of gravity waves from fronts by calculating the linear, low-frequency gravity wave response to a forcing modeled on the cross-front acceleration neglected by SG. Although neglecting all nonuniformity of the flow near the front and specifying a priori the structure of the crossfront acceleration, their calculations did suggest that the terms neglected by SG will always force gravity waves. Gall et al. (1988) hypothesized that the forcing of waves by the frontogenesis could excite standing waves in the cold air beneath the surface front and that these resonant waves would in turn corrugate the frontal surface and provide the horizontal scale for the stationary waves above the front. The importance of gravity wave emission was questioned by G89, who

conjectured instead that "nonwavy imbalances" were primarily responsible for the differences between his frontogenesis simulations and SG solutions. These nonwavy imbalances would be the next-order corrections to SG in an expansion of the PE for small cross-front flow, and as such are distinct from freely propagating gravity waves. Other work has focused on extending SG solutions beyond frontal collapse, either by incorporating singularities into SG solutions (e.g., Cullen and Purser 1984; Koshyk and Cho 1992) or by ad hoc parameterization of diffusion and wave dispersion within an internal boundary layer associated with the front (Blumen 1992). In either case, such studies do not directly address the effect of the neglect of the cross-front acceleration by SG.

Thus, in what follows we ask if frontal dynamics can, for very intense fronts, differ substantially from the SG paradigm, and if so, whether emitted gravity waves account for a significant portion of the differences. We examine these questions in the context of two model problems, the deformation- and shear-induced fronts. The physical description of the model problems is given in section 2, along with an outline of the numerical methods used in the integrations. In order to isolate the effects of the cross-front accelerations neglected by SG, the fronts considered here are two-dimensional and nearly adiabatic and inviscid except very near and following frontal collapse, when explicit horizontal diffusion is included in the numerical model to limit the scale contraction of the solutions. Other effects that will likely produce differences from SG dynamics, such as boundary-layer processes and alongfront variability or instabilities, are ignored. Discussion of the results is divided into three parts: inviscid, precollapse solutions at moderate resolution in section 3, postcollapse solutions with explicit horizontal diffusion in section 4, and solutions with high spatial resolution in section 6. Along the way, we identify gravity waves associated with two distinct physical sources, those generated "externally" by temporal variations in the frontogenetical forcing and those generated internally by the intensity of the frontal circulation, as well as more familiar but spurious waves associated with model initialization and insufficient resolution. When spurious gravity waves are eliminated, SG provides a good approximation of the model fronts. Section 5 provides some brief analysis both of the higher-order corrections to SG and of the gravity wave emission. We show that emitted gravity waves should · be noticeable away from the front before the SG solution becomes invalid and that, at least in some of the cases examined here, the higher-order corrections to the SG cross-front circulation are substantially smaller than the emitted gravity waves. Our results are summarized in section 7.

An understanding of the behavior of inviscid fronts near collapse or diffusion-limited fronts following collapse is of more than academic interest. Although no

case of gravity wave emission from a front has been documented observationally, gravity waves (or other wavelike disturbances) have appeared in high-resolution simulations of baroclinic waves and have been hypothesized to contribute to the mesoscale banding of cloud and precipitation in midlatitude cyclones (Polavarapu and Peltier 1990; Tremblay 1992). Furthermore, both model simulations and operational mesoscale forecasts now routinely achieve horizontal resolutions of less than 15 km, but there is little in the way of either observations or theory upon which to judge such numerical solutions. In the above cases, it is also likely that the simulation or forecast of frontogenesis is at least partially controlled by explicit horizontal diffusion.

2. Model problems and numerical methods

a. The physical problems

We consider two frontal problems, the deformation-induced front and the shear-induced front within an Eady wave, formulated as in Hoskins and Bretherton (1972) and Williams (1967), respectively. Both these fronts are two-dimensional in the sense that the frontal flow is strictly independent of the alongfront coordinate.

Adopting x and y as the Cartesian coordinates across and along the front, the flow in both cases consists of a known background flow $(\bar{u}, \bar{v}, \bar{\theta})$ plus y-independent perturbations, which will be denoted by lowercase variables without an overbar. For the deformation front,

$$\bar{u} = -\alpha x, \quad \bar{v} = \alpha y, \quad \bar{\theta} = (\theta_0/g)N^2 z, \quad (1a)$$

where $\alpha = \alpha(t)$ is the deformation rate, N^2 is a constant ambient static stability, and $\theta_0 = 300$ K. Frontogenesis is forced by this deformation flow acting on an initial potential temperature field $\theta(x, z)$ and an associated alongfront wind $v(x, z)$. The background flow for the shear front is the Eady (1949) basic state for baroclinic instability:

$$\bar{u} = \Lambda z, \quad \bar{v} = 0, \quad \bar{\theta} = \frac{\theta_0}{g}(-f\Lambda y + N^2 z), \quad (1b)$$

where Λ is the constant vertical shear. A developing Eady wave then provides the horizontal shear [in $v(x, z)$] and differential temperature advection that force the frontogenesis.

The frontal flow is governed by the Boussinesq equations,

$$\frac{d\mathbf{v}}{dt} + \mathbf{v} \cdot \nabla\bar{\mathbf{v}} + f\mathbf{k} \times \mathbf{v} = -\nabla\phi + \frac{g\theta}{\theta_0}\mathbf{k} + \nu\mathbf{v}_{xx}, \quad (2a)$$

$$\frac{d\theta}{dt} + \mathbf{v} \cdot \nabla\bar{\theta} = \nu\theta_{xx}, \quad (2b)$$

$$\frac{d\phi}{dt} = -c_s^2\nabla \cdot \mathbf{v}, \quad (2c)$$

where $\phi = c_p\theta_0(p/p_0)^{(\gamma-1)/\gamma}$, ν is the artificial horizontal diffusion coefficient for all frontal variables, c_s is the sound speed, $d/dt = \partial_t + (\bar{u} + u)\partial_x + w\partial_z$, and other notation is conventional. Although the motions studied here are nearly anelastic and hydrostatic, the compressible continuity equation (2c) and the nonhydrostatic accelerations in (2a) are retained for computational reasons.[1]

For either front, the flow is confined between rigid horizontal boundaries at $z = 0, H$ and will have uniform PV initially, where the PV is given by

$$q = \rho_0^{-1}[f\mathbf{k} + \nabla \times (\bar{\mathbf{v}} + \mathbf{v})] \cdot \nabla(\bar{\theta} + \theta), \quad (3)$$

with $\rho_0 = 1$ kg m^{-3}. Lateral boundary conditions are decay of the frontal variables as $|x| \to \infty$ for the deformation front, and periodicity for the shear front.

Specific instances of both the deformation- and shear-induced fronts will be examined in detail. The initial v and θ fields for the deformation front are obtained, as discussed in section 2b, by inverting the uniform interior PV for ϕ subject to the geostrophic coordinate boundary conditions

$$\theta = (\Delta\theta/\pi)\tan^{-1}X/L, \quad z = 0, H, \quad (4)$$

where $X = x + f^{-1}v_g$. We use the following values for various parameters: $\Delta\theta = 13.8$ K, $L = 360$ km, $H = 9$ km, $\alpha = 0.2f = 2 \times 10^{-5}$ s^{-1}, and $N^2 = 3.76 \times 10^{-5}$ s^{-1}, which gives an initial PV of 0.115 PVU. With these choices, our solutions may be directly compared with the "moderate PV" case of G89; the initial v and $\theta + \bar{\theta}$ fields are shown in his Fig. 4a.

For the shear front, the basic state has vertical shear $\Lambda = 3 \times 10^{-3}$ s^{-1} and stratification $N^2 = 0.981 \times 10^{-4}$ s^{-2}. The resulting values of the y-temperature gradient and interior PV are -0.92 K/100 km and 0.272 PVU, respectively. The domain has horizontal periodicity of 4000 km and depth $H = 10$ km.

b. The numerical model

We integrate the nonhydrostatic equations (2) as described in Skamarock and Klemp (1992) using a quasi-compressible time-split scheme based on that of Klemp and Wilhelmson (1978). Briefly, the equations are differenced on a spatially staggered grid with velocity components u_i located one half Δx_i from the (ϕ, θ) points; spatial derivatives are calculated with second-order centered differencing. To maintain computational efficiency, the pressure gradient terms, the divergence term, the buoyancy term in (2a), and the

---

[1] When $\alpha(t)$ is not a constant, the background flow given by (1a) is not an exact solution of the compressible equations. However, the compressible corrections to (1a) are small for typical values of α and $d\alpha/dt$.

vertical advection of the horizontally averaged potential temperature in (2b) are integrated with small time steps stable for the acoustic modes using a scheme that is semi-implicit in the vertical. All other terms are integrated over a large time step that is limited only by the advection velocity. Other than the horizontal diffusion, the only explicit dissipations in the numerical model are a filter on the leapfrog time step following Robert (1966) and "divergence damping" terms in the x- and z-momentum equations following Skamarock and Klemp (1992).

The periodic lateral boundary conditions for the Eady wave are trivial to implement numerically, but the decay conditions required for the deformation front are problematic given a limited computational domain. Most PE simulations of the deformation front have simply fixed the frontal variables at their initial values on the lateral boundaries (Williams 1972; Keyser and Pecnick 1985; Koclas et al. 1986). We find that these boundary conditions generate gravity waves with amplitudes large enough to complicate the identification of gravity waves from other sources. Our current choice of boundary conditions follows Klemp and Wilhelmson (1978) for u, v, w, and ϕ: x derivatives of v and w are set to zero at inflow boundaries and calculated by one-sided differences at outflow boundaries, a radiation condition (using the phase speed of the gravest internal mode) is applied for u, and no conditions are imposed on ϕ. The time tendency of θ at the lateral boundaries, in contrast, is set equal to its value one grid point inward. As long as the initial baroclinity is concentrated away from the lateral boundaries, the choice of boundary condition for θ makes little difference in the evolution of v and θ in the interior. These boundary conditions do, however, significantly reduce the generation of gravity waves over the initial 12–36 h.

The initial conditions for the deformation front simulations consist of an alongfront jet and potential temperature distribution in thermal wind balance, together with a frontal circulation (u, w) diagnosed from the Sawyer–Eliassen equation (Sawyer 1956; Eliassen 1962). In essence, the model is initialized with the SG solution at a given time.

Specifically, θ is first calculated in geostrophic coordinates, given its distribution on the boundaries, by inverting the PV equation. After transforming θ to the physical grid, ϕ and v are calculated from the hydrostatic and geostrophic relations, respectively. The ageostrophic streamfunction ψ is then calculated from the Sawyer–Eliassen equation

$$(g\bar{\theta}_z/\theta_0 + \phi_{zz})\psi_{xx} - 2\phi_{xz}\psi_{xz} + (f^2 + \phi_{xx})\psi_{zz}$$

$$= \begin{cases} -2\alpha\phi_{xz}, & \text{for the deformation front} \\ -2\Lambda\phi_{xx}, & \text{for the shear front.} \end{cases} \quad (5)$$

This is derived from (2) by assuming thermal wind

balance for v and θ and forming $f\mathbf{j}\cdot\partial_z(2a) - (g/\theta_0)\partial_x(2b)$. Defining ψ on a grid staggered by one-half grid interval in each coordinate direction from the ϕ points, we use successive overrelaxation to solve (5) subject to

$$\psi = 0 \text{ on } z = 0, H \text{ and } \frac{\partial\psi}{\partial x} = \pm\mu\psi \text{ on } x = \mp x_B,$$

where $x = \pm x_B$ are the lateral boundaries and $\mu^2 \equiv \theta_0 f^2 \pi^2/(g\bar{\theta}_z H^2)$. Use of the approximate decay condition above also helps to reduce the initial pulse of gravity waves from the lateral boundaries.

The shear front simulations are initialized with a small-amplitude $(0.1 \text{ m s}^{-1} \text{ in } v)$ balanced disturbance, from which the most unstable Eady wave rapidly emerges. Once the wave reaches large amplitude, its development and the associated frontogenesis are independent of the initialization.

Since the flow variations may rapidly collapse to the grid scale in the vicinity of the front, the numerical solutions are checked to ensure that truncation errors remain negligible. This is achieved either by verifying, when computationally feasible, that the solutions are grid independent, or by simply monitoring the PV for spurious anomalies. (A given feature of a solution is "grid independent" if it is unchanged by a doubling of *both* the horizontal and vertical resolution.) Experience indicates that PV conservation is the more stringent test, in that noticeable PV anomalies appear before any features of interest become dependent on the grid spacing. In what follows, we will discuss only those aspects of the numerical solutions that have at least passed the grid-independence test.

Before differences between PE and SG fronts can be understood, it is necessary to define reference SG fields with which to compare the PE solutions. In order to focus on how the PE and SG dynamics differ near frontal collapse (rather than on how small errors accumulate in a prognostic SG simulation), we choose to diagnose SG fields from the instantaneous PV distribution in the PE solutions. Orlanski and Ross (1977) briefly consider a similar but less systematic approach.

Denoting the diagnosed SG variables with the subscript *sg*, the algorithm begins with the calculation of ϕ_{sg} from the PV distribution via

$$\left(f^2 + \frac{\partial^2\phi_{sg}}{\partial x^2}\right)\left(\frac{g}{\theta_0}\frac{\partial\bar{\theta}}{\partial z} + \frac{\partial^2\phi_{sg}}{\partial z^2}\right) - \left(\frac{\partial^2\phi_{sg}}{\partial x\partial z}\right)^2$$

$$= \frac{fg}{\theta_0}\left(\rho_0 q - \frac{\partial\bar{u}}{\partial z}\frac{\partial\bar{\theta}}{\partial y}\right), \quad (6a)$$

with the boundary conditions

$$\frac{\partial\phi_{sg}}{\partial z} = \frac{g}{\theta_0}\theta, \quad z = 0, H. \quad (6b)$$

Note that q is the total PV, given by (3). This yields the mass field that, subject to the cross-front geostrophic

balance assumed by SG, is consistent with q. [When cross-front geostrophic balance is assumed, the analog of PV conserved by the SG equations is as in (6a), i.e., it does not involve the alongfront component of vorticity (Hoskins and Bretherton 1972).] Again, (6) is solved using successive overrelaxation with ϕ_{sg} defined on the same grid as ψ and the boundary conditions (6b) evaluated using θ at the lowest and uppermost grid levels from the PE solution. Given ϕ_{sg}, the SG ageostrophic circulation is obtained from (5), after replacing ϕ with ϕ_{sg}. In general, some adjustment of the volume average of q is necessary so that (6) is solvable, but the adjustments are small and the diagnosed secondary circulation (u_{sg}, w_{sg}) is not sensitive to this process.

3. Inviscid fronts near collapse

a. Deformation fronts with constant α

First consider the deformation-induced front, as in G89. The simulations discussed in this section have moderate resolution, using horizontal and vertical grid spacings of 25 km and 225 m, and use a computational domain with $x_B = 2700$ km. The relative grid spacing is motivated by the SG solution, for which the ratio of vertical to horizontal scales is roughly $f/N \sim 0.01$.

Figure 1a shows the vertical velocity and potential temperature after 16 h, 40 minutes prior to the collapse predicted by SG. As the front has intensified, the maximum ascent has increased from 1.2 cm s^{-1} at $t = 0$ to 3.2 cm s^{-1}, and its location has dropped toward the surface front. At this time, v (not shown; see Fig. 4b in G89) varies from -32 m s^{-1} at the surface to 32 m s^{-1} at the lid.

The vertical velocity is smooth near the center of the domain but, away from the center, a variety of ripples are visible in the isolines. This solution agrees well with that of G89, as can be seen by comparing Fig. 1 to his Fig. 5b, which depicts w at 16.7 h. In fact, if our simulation is continued to 16.7 h, the frontal updraft splits into two distinct maxima as in G89, although even at 16 h our gridpoint solution does not resolve the most intense portion of the fronts and possesses significant positive PV anomalies where the fronts intersect the horizontal boundaries.

The diagnosed SG vertical velocity, shown in Fig. 1b, resembles the model w in both magnitude and general structure but lacks any "bumps." The difference field, $w - w_{sg}$ (Fig. 1c), reveals that the bumpiness in w has a distinct spatial structure. The dominant features are a sequence of updrafts and downdrafts having the vertical structure of the gravest mode (vertical wavelength $2H$) and extending from the frontal nose at $x \approx 400$ km laterally away from the front past $x = 800$ km. Closer inspection, however, also hints at features almost directly above the frontal nose that have the form of the second mode in z, with vertical wavelength H.
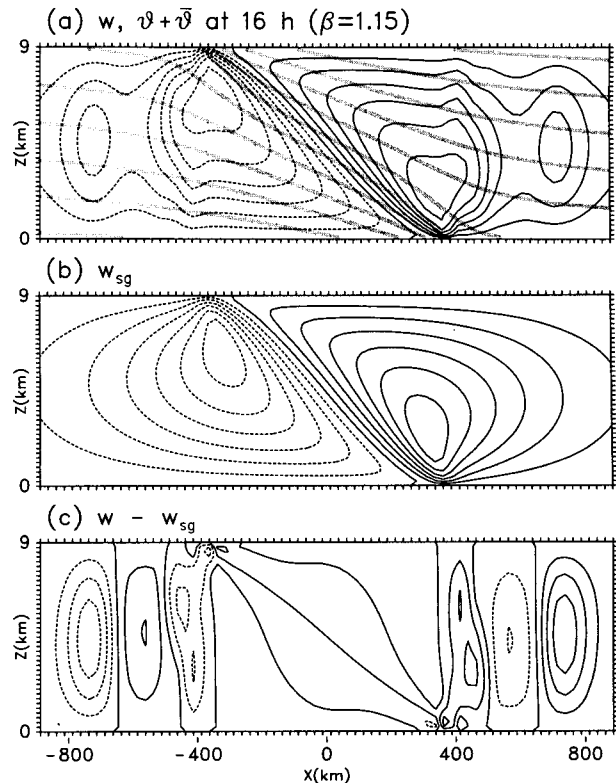

FIG. 1. Deformation front at 16 h ($\beta = 1.15$), using parameters of G89: (a) w (contour interval 0.5 cm s^{-1}) and θ (heavy gray lines, contour interval 2 K), (b) w_{sg} (contour interval 0.5 cm s^{-1}), and (c) $w - w_{sg}$ (contour interval 0.2 cm s^{-1}). Only the central 1800 km of the computational domain is shown, and tick marks denote grid points.

If the disturbances in Fig. 1c are gravity waves, they must be approximately hydrostatic because of their horizontal scale and, in a uniform medium, will be horizontally nondispersive and have phase speed $c = N/m$, where m is the vertical wavenumber. If such waves are embedded in a deformation flow given by (1a), they will, to a first approximation, propagate toward their "stationary line" at $x = N/(\alpha m)$ with speed $-\alpha x + N/m$ (Jones 1969). Both the horizontal wavelength following a wave packet and the distance between a packet and its stationary location decrease as $\exp(-\alpha t)$. Neglecting effects of the frontal flow on the wave propagation, the gravest and first internal modes in these simulations have phase speeds ± 17.6 m s^{-1} and ± 8.8 m s^{-1}, respectively, and for $\alpha = 0.2f$ have stationary lines at $x = \pm 880$ km and $x = \pm 440$ km, in good agreement with the locations of the disturbances in Fig. 1c of vertical wavelength $2H$ and H.

The nature of these disturbances can be more conclusively determined by examining their dependence on α and comparing with the behavior expected of gravity waves. Figure 2 shows w, w_{sg}, and $w - w_{sg}$ for a simulation with $\alpha = 0.1f$, $x_B = 5400$ km, and begin-
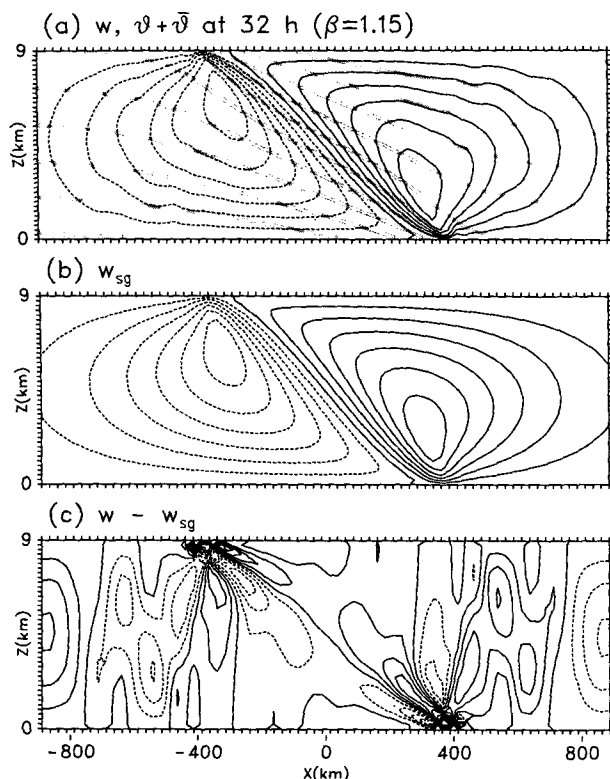
(a) w, $\vartheta + \bar{\vartheta}$ at 32 h (β=1.15)

(b) w_{sg}

(c) $w - w_{sg}$

FIG. 2. Deformation front with $\alpha = 0.1f$ at 32 h ($\beta = 1.15$): (a) w (contour interval 0.25 cm s^{-1}) and θ (heavy gray lines, contour interval 2 K), (b) w_{sg} (contour interval 0.25 cm s^{-1}), and (c) $w - w_{sg}$ (contour interval 0.025 cm s^{-1}). All parameters are as in Fig. 1 except $\alpha = 0.1f$.

ning from initial conditions given by (4). (For comparison with the $\alpha = 0.2f$ case, this simulation is continued to 32 h, since the SG solutions have the property that v and θ, and the spatial structure of u and w, depend only on the integrated deformation $\beta = \int_0^t \alpha dt'$.) With α and the background deformation flow reduced by half, any gravity waves present should propagate roughly twice as far from the front. This behavior can be seen in Fig. 2, where the disturbances have moved significantly farther away from the front, the gravest modes having propagated almost out of the figure and the modes of vertical wavelength $2H$ spreading over a region 300 km wide. We conclude that internal waves are by far the largest contributors to $w - w_{sg}$.[2]

Based largely on the agreement between the observed location and that predicted by linear wave theory, G89

---

[2] Other prominent features in Fig. 2c include an updraft–downdraft couplet that slopes along the frontal surface and structures near the frontal nose with scales comparable to the grid scale. Because the nose of the front is poorly resolved at this time, these features depend on the grid spacing, reflecting truncation errors in both the model solution and the diagnosis of w_{sg}. However, the waves propagating away from the front do not depend on the model resolution.

also attributes the isolated maximum in w near $x = 800$ km to the gravest internal wave (possibly generated by the model initialization), and notes that waves of wavelength H may be responsible for some of the ripples in w above the nose of the surface front. However, he suggests that the splitting of the frontal updraft is not associated with freely propagating gravity waves but instead is due to a higher-order correction to the SG solution. The balanced corrections to SG are discussed in section 5, but it is apparent in this case that propagating gravity waves account for most of the differences from the SG solution.

The propagation characteristics of these waves are further illustrated in Fig. 3, which displays the wave amplitude

$$a_n(x, t) = (2H)^{-1} \int_0^H (w - w_{sg}) \sin(n\pi z/H) dz, \quad (7)$$

for $n = 1, 2$ and $\alpha = 0.2f, 0.1f$. There are clear signals of wave propagation away from the front and toward the predicted stationary lines (indicated by gray vertical lines), except in the case of the second mode for $\alpha = 0.2f$ where the waves are trapped within the frontal region and are nearly stationary at $x = 400$ km. In qualitative agreement with ray-tracing arguments, the propagation slows and the horizontal wavelengths decrease near the stationary lines. Note also the weak pulses propagating inward from the lateral boundaries.

b. Variable deformation, $\alpha = \alpha(t)$

All the waves shown in Fig. 3 exist with significant amplitude even at early times. This is contrary to what would be expected if the accelerating frontogenesis were the generating mechanism and suggests that much of the wave energy is a spurious result of the model initialization.

The influence of the numerical initialization may be lessened by allowing the deformation rate to slowly increase from zero as a function of time, since the initial geostrophically balanced alongfront jet with u, w, and α all zero is a known, wave-free solution to the equations. We choose the following time dependence for α:

$$\alpha(t) = \alpha_f[1 - \exp(-t^2/\tau^2)], \quad (8)$$

which provides a smooth transition from $\alpha = d\alpha/dt = 0$ initially to the final value of α_f. Although beginning the integrations with $\alpha = 0$ eliminates any waves associated with the initial conditions, the time variation of α may result in production of gravity waves; consider, for example, the limit $\tau \to 0$.

Difference fields $w - w_{sg}$ are shown in Fig. 4 for two simulations with $\alpha_f = 0.1f$, the first using $\tau = 1$ d and the second $\tau = 0.5$ d. The integrations continue until the integrated deformation $\beta = 0.2f \times (16 \text{ h}) = 1.15$,
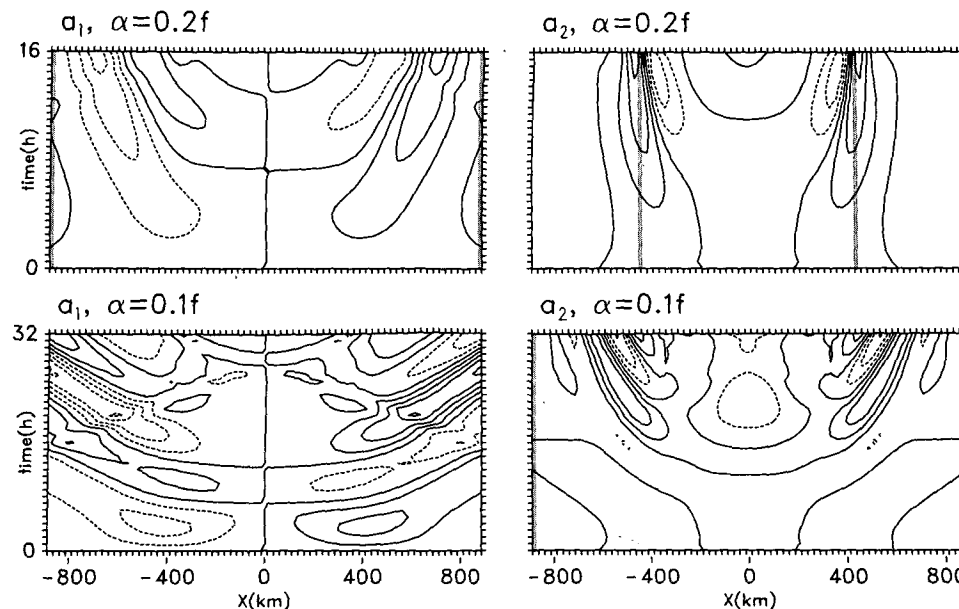
FIG. 3. $a_1(x, t)$ and $a_2(x, t)$ [defined by (7)] for the deformation-front simulations with $\alpha = 0.2f$ (top panels: contour interval 0.2 cm s^{-1} for a_1 and 0.05 cm s^{-1} for a_2) and $\alpha = 0.1f$ (bottom panels: contour interval 0.025 cm s^{-1} for a_1 and 0.0125 cm s^{-1} for a_2). Vertical gray lines indicate the approximate locations at which the modes are stationary.

so that the solutions are directly comparable with the constant α case shown in Fig. 2. Gravity waves are present in both simulations and their amplitude depends strongly on τ, with wave amplitudes increasing by nearly a factor of six as τ decreases from 1 d (Fig. 4a) to 0.5 d (Fig. 4b). Hence, these waves are likely produced by the time variation of α and would presumably vanish for sufficiently large τ. In addition,
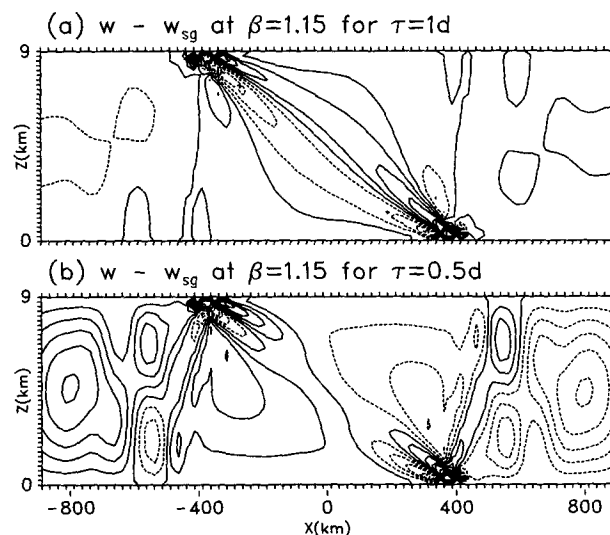

FIG. 4. $w - w_{sg}$ (contour interval 0.025 cm s^{-1}) for the deformation front with variable α; $\alpha(t)$ is given by (8) with $\alpha_f = 0.1f$ and $\tau = 1$ d (a) or $\tau = 0.5$ d (b).

wave amplitudes for $\tau = 1$ d are roughly one-third of those in the constant deformation case, again indicating that the waves shown in Figs. 1 and 2 arise largely from the model initialization.

Regardless of their source, the gravity waves represent a small correction to the SG solution when $\tau = 1$ d. The maximum in w, for example, is more than 1.5 cm s^{-1}, while the maximum in $w - w_{sg}$ away from the frontal surface (where truncation errors in the diagnostic calculations overwhelm the physical signal) is 0.034 cm s^{-1}. Thus, in this case, there is little difference between the PE and SG dynamics up to an hour before frontal collapse (as will be confirmed by higher-resolution simulations in section 6), and in particular, none of the deviations from the SG solution noted by G89 or GWC are present.

c. Shear-induced fronts

Since initializing the Eady wave with sufficiently small perturbations eliminates gravity wave sources in the model initialization, simulations of shear-induced fronts can be used to check some of the above conclusions. The basic integration begins with initial conditions and parameter choices as in section 2. The vertical and horizontal grid intervals are 0.3125 km and 31.25 km, respectively, and again have a ratio of roughly f/N.

Eight days after initialization, a strong front has formed within the Eady wave, as illustrated by the θ field in Fig. 5a. The vertical velocity (also Fig. 5a) has
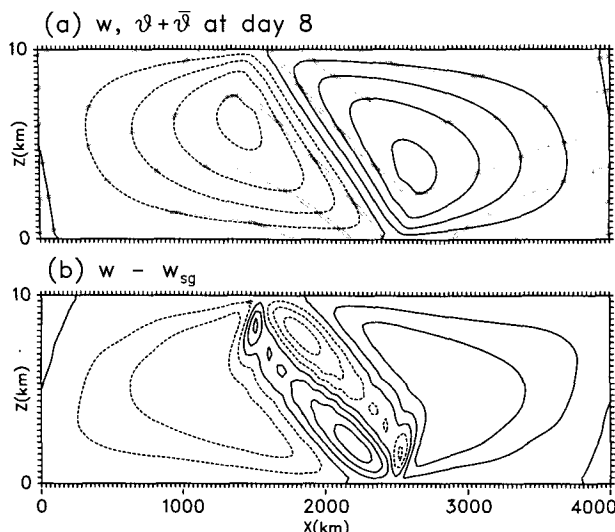
(a) w, $\vartheta + \bar{\vartheta}$ at day 8

(b) w − w$_{sg}$

FIG. 5. Eady wave at day 8, using parameters of section 2: (a) w (contour interval 1 cm s^{-1}) and θ (heavy gray lines, contour interval 10 K), (b) $w - w_{sg}$ (contour interval 0.1 cm s^{-1}). The full, horizontally periodic domain is shown and tick marks denote grid points.

magnitude and structure similar to that in the deformation front, and the alongfront wind (not shown) varies ±48 m s^{-1}. Other integrations with initial conditions of different amplitudes produce essentially identical solutions, though of course the time required depends on the initial amplitude.

For an Eady wave with a 4000-km wavelength, SG theory predicts frontal collapse when the alongfront geostrophic wind, $v_g = f^{-1}\phi_x$, reaches 64 m s^{-1}. In the model, v_g should reach this amplitude at roughly day 8.4, if we use the growth rate of the Eady wave in the model to extrapolate forward from day 8. Consistent with the SG prediction, the model solution is adequately resolved at day 8, yet signs of truncation errors soon indicate that the front has collapsed past the grid scale: a weak local maximum in the PV appears at the nose of the front within the next hour and continues to grow rapidly to a maximum value of nearly 0.3 PVU by day 8.2. Doubling both the horizontal and vertical resolution delays the onset of PV generation by less than two hours. Hence, as in the deformation front, SG frontal collapse coincides broadly with the loss of resolution in the model simulation.

The contours of w exhibit noticeable ripples, though compared to the gravity waves in the simulations of the deformation front, these disturbances are more localized near the surface and upper-level fronts (compare Figs. 1 and 5) and propagate slowly, if at all, relative to the fronts. Consideration of $w - w_{sg}$ (Fig. 5b) reveals that the disturbances are not present in the SG solution. Again, as in the deformation front, the disturbances amount to only small corrections to the SG fields and have no obvious correspondence to the de-

viations from SG noted by G89 and GWC. However, unlike the deformation front, the disturbances do not depend on the model initialization and must therefore arise from the internal dynamics of the Eady wave and front. (Because the front is near collapse at day 8, diagnostic quantities such as $w - w_{sg}$ depend weakly on the resolution. Nevertheless, halving both grid intervals increases the magnitude of $w - w_{sg}$ by 20%, but does not affect the spatial structure.)

Superimposed on the smaller-scale wavelike disturbances in $w - w_{sg}$ is a component with similar amplitude but having scales comparable to that of the Eady wave, suggesting that both emitted waves and higher-order corrections to SG are present. Consistent with the interpretation that the two components have different origins, the larger-scale component exists even before significant frontogenesis has occurred and gradually increases with time, while the small-scale downdraft near the surface front (and the corresponding updraft near the lid) does not appear until just prior to collapse.

4. Fronts with dissipation following collapse

The diagnostic SG solution provides a good approximation to the model solutions in the foregoing inviscid simulations. In particular, no counterpart to the stationary gravity waves of GWC appears in the simulations, and the deviations from SG noted by G89 turn out to be gravity waves associated with imperfect initialization of the model, rather than being inherently produced by the internal dynamics of the front.

However, there are indications from the shear-front simulation that, as collapse approaches, small deviations from SG are generated by the frontogenesis. These deviations should increase as the cross-front scale contracts and the cross-front acceleration increases, as discussed in section 1. Unfortunately, the contraction of the frontal scale also means that truncation errors must, at some point, begin to influence the numerical simulation. Increasing the resolution can extend the inviscid solutions closer to the time of SG collapse, yet in practice the frontal scale decreases rapidly enough that little extra time is gained.

In order to focus on the deviations that arise from the internal dynamics of the front, we add explicit horizontal diffusion to the simulations [i.e., $\nu \neq 0$ in (2)]. Although dissipative processes may limit frontal collapse in the atmosphere, choosing the dissipation to have the form of horizontal diffusion has little physical justification and is at best a simple model of the actual physics. Nevertheless, adding diffusion allows the solutions to be integrated beyond the inviscid frontal collapse and enables us, at least in specific cases, to demonstrate more conclusively the nature of differences between the model and SG dynamics. Besides limiting the cross-front scale, the presence of diffusion also has

the advantage that the simulations are less sensitive to the model initialization. We examine below both the continued intensification of frontogenesis within the Eady wave, which is accompanied by substantial increases in wave emission, and the eventual steady state of the dissipative deformation front.

a. Shear-induced fronts with dissipation

The simulations of the "viscous" shear front are identical to the inviscid simulations, except $\nu = 10^5$ m^2 s^{-1} is used in (2) and results will be shown for simulations with horizontal and vertical grid spacings of 15.6 km and 156 m, respectively. The simulations with diffusion begin from the inviscid solution at day 8, which is well resolved at that time.

By day 9 (i.e., after one day with $\nu \neq 0$), the maximum vertical velocity has increased to more than 16 cm s^{-1}, as shown in Fig. 6a, and the alongfront velocity (not shown) varies ± 90 m s^{-1}. With the continued growth of the baroclinic wave, the frontal updraft has split into an intense upward jet at the nose of the front and secondary maximum aloft over the frontal surface. The Eady wave reaches its maximum amplitude as measured by $|v|$ somewhat after day 10, when the wave "equilibrates" as described by Nakamura and Held (1989).

Near the front, local dissipative effects are evident in the limitation of the front to resolvable scales—at day 9, the solution with horizontal diffusion is smooth and grid independent, while the inviscid integration (not shown) is dominated by numerical noise. In addition, with dissipation PV is no longer materially conserved and, as shown in Fig. 6b, positive PV anomalies with magnitudes of more than 20 PVU develop at the fronts by day 9. Although our simulations use purely horizontal diffusion, the anomalies are similar in structure to those found by Nakamura and Held (1989) using a full ∇^2 diffusion.

The generation of positive PV within the frontal zone may be qualitatively understood from the PV equation for (1),

$$\frac{dq}{dt} = -\nabla \cdot \mathbf{F},$$

where the PV flux is $\mathbf{F} = -\nu(\theta_{xx}\zeta + \theta\zeta_{xx})$. The flux divergence is nonzero wherever there are gradients in heating along vortex lines or gradients in potential temperature along the curl of the momentum forcing. Near the surface front, θ_{xx} is negative (Hoskins and Bretherton 1972) and all gradients decay upward. Assuming that $\zeta_{xx} \approx -l^2\zeta$, where l is a cross-front length scale, both terms in $\mathbf{F}$ then parallel the vorticity vector and decrease upward. Since ζ points into the domain near the surface front, there is a convergent flux of PV into the domain, resulting in the generation of a positive PV anomaly. Similar arguments hold for the front at the lid.
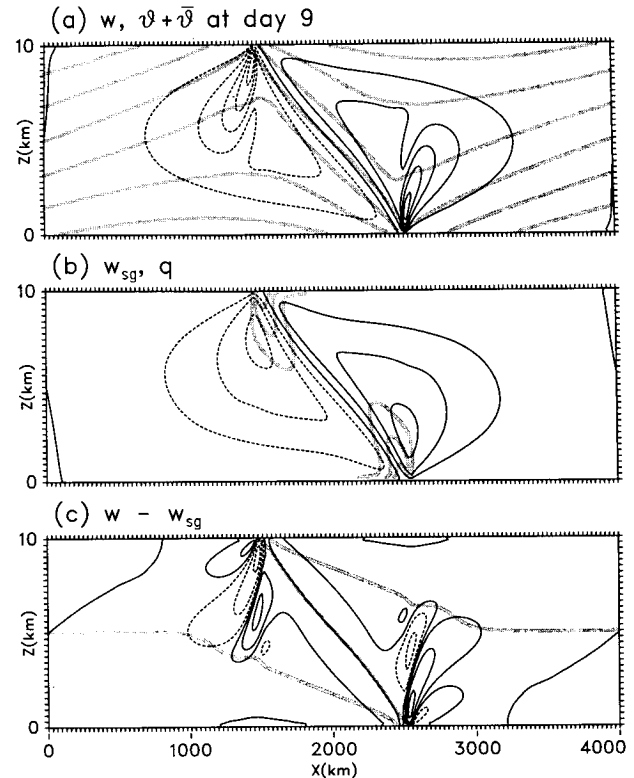

FIG. 6. Eady wave at day 9, with horizontal diffusion turned on since day 8: (a) w (contour interval 3 cm s^{-1}) and θ (heavy gray lines, contour interval 15 K), (b) w_{sg} (contour interval 3 cm s^{-1}) and q (heavy gray lines, contours at 1, 4, 10 PVU), and (c) $w - w_{sg}$ (contours at 1, 3, 6 cm s^{-1}). In (c), the critical surface for the waves ($\bar{u} + u = 0$) is shown in gray. Tick marks appear every 2 grid points.

Figures 6b,c display w_{sg} and $w - w_{sg}$, respectively. While the SG vertical velocity has the smooth, wedge-shaped structure familiar from the inviscid fronts, the difference field $w - w_{sg}$ is dominated by narrow [O(75 km)] plumes of ascent and descent stacked above the nose of the surface front. In addition, w_{sg} and $w - w_{sg}$ now have nearly the same magnitude, in contrast to the situation one day earlier. Quantitative changes in $w - w_{sg}$ occur gradually as the integration continues and the Eady wave evolves, yet the general pattern remains fixed relative to the Eady wave without evidence of horizontal propagation.

Although SG predicts that localized PV anomalies near a front can produce ripples in the vertical velocity (Chan and Cho 1989), the smoothness of w_{sg} indicates that such effects are weak in this case, so that the disturbance is due to dynamics neglected by SG. In fact, the differences between w and w_{sg} appear to be due to a gravity wave: its specific characteristics, such as the phase tilts into the flow with height and the confinement of wave amplitude to a restricted horizontal domain above the front, are consistent with an approximately hydrostatic and stationary wave propagating

upward from a source near the nose of the front. Estimating the mean $\bar{u} + u$ and N in the "wavy" layer to be 10 m s^{-1} and 1.2×10^{-2} s^{-1}, respectively, the hydrostatic dispersion relation for stationary internal waves predicts a vertical wavelength of $N/(\bar{u} + u)$ ≈ 7.2 km, in fair agreement with the wavelength of the disturbance. Furthermore, since the wave is approximately stationary, it has a critical surface where $\bar{u} + u = 0$, which is indicated by a gray line in Fig. 6c. The decrease in the vertical wavelength below the critical surface, which is evident in the curving of the phase lines toward the horizontal, and the vanishing of wave amplitude above the critical surface are also consistent with an upward-propagating stationary wave that is absorbed near the critical surface.

We have verified that this numerical solution is well resolved (by producing virtually identical simulations at both doubled and halved spatial resolutions) and is qualitatively independent of the time at which the horizontal dissipation is turned on. Thus, we conclude that the frontogenesis is forcing gravity waves. Questions remain concerning the role of the horizontal diffusion, since the emitted waves depend on the magnitude of the diffusion (their amplitude increasing and their horizontal scale shrinking as the diffusion is reduced) and the inviscid simulations exhibit only a hint of similar waves. Below, we will suggest that the diffusion's primary role is to determine the minimum scale of the front.

The internal wave shown in Fig. 6c is in some ways reminiscent of the stationary waves above the frontal surface in the simulations of Gall et al. (1988). However, Gall et al. also find standing waves trapped beneath the front that, they suggest, corrugate the frontal surface and set the scale for the waves above the front. Our solutions exhibit no counterpart to these standing waves.

b. Nearly steady deformation fronts

In the presence of dissipation, the deformation front reaches a steady state in which the frontogenetical effects of the large-scale deformation are balanced by dissipation (Williams 1974). Unlike the inviscid solutions, this steady state contains no remnant of the gravity waves generated by the model initialization.

Choosing a horizontal diffusion of $\nu = 10^5$ m^2 s^{-1} but otherwise using the G89 parameters, our simulations of the deformation front reach a nearly steady state by 48 h. The solutions are not completely steady, since there is a slow [O(1 m s^{-1})] translation of the fronts outward from $x = 0$. We present results for a horizontal grid spacing of 12.5 km and, because the diffusion strongly damps gravity waves produced at the lateral boundaries, we return to the simple conditions that all variables are permanently fixed at their initial values at the lateral boundaries.

The vertical velocity and θ, and the alongfront ve-

locity and PV, are shown at 48 h in Fig. 7. As in the postcollapse Eady wave, the steady-state frontal updraft splits into two distinct maxima (Fig. 7a) and large-amplitude PV anomalies develop along the frontal surface (Fig. 7b). The split in w again results in an ascending jet at low levels near the frontal nose.

Once again, the diagnosed w_{sg} is smooth and deviations from the SG solution account for most of the structure in w above the frontal nose, as shown in Fig. 7c. In this case, $w - w_{sg}$ is a relatively small correction, with a magnitude of less than 1 cm s^{-1} compared to 5 cm s^{-1} for w_{sg}. The structure of $w - w_{sg}$ is dominated by a disturbance of vertical wavelength H, located above the frontal nose; this vertical wavelength is again consistent with a stationary hydrostatic gravity wave. (Recall from the inviscid simulations that the "initialization" waves of vertical wavelength H were stationary almost directly above the surface front when $\alpha = 0.2f$.) The weak phase tilts with height indicate that the stationary wavelength and the depth of the domain are close enough for a standing wave to form.

Thus, it appears that gravity waves again contribute strongly to the differences between the model and SG solutions. The waves have scales somewhat greater than
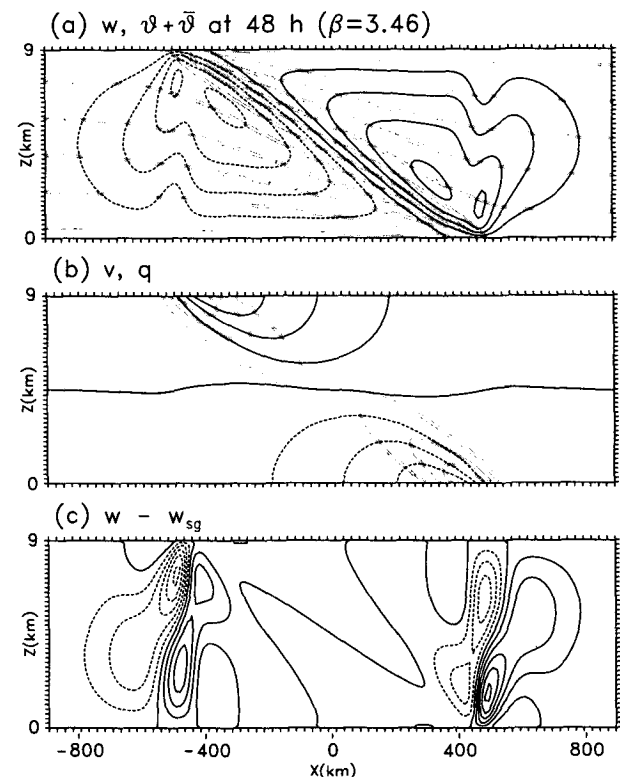
(a) w, $\vartheta + \bar{\vartheta}$ at 48 h $(\beta = 3.46)$

(b) v, q

(c) $w - w_{sg}$

FIG. 7. Deformation front with horizontal diffusion (other parameters as in G89) at 48 h $(\beta = 3.46)$: (a) w (contour interval 1 cm s^{-1}) and θ (heavy gray lines, contour interval 2 K), (b) v (contour interval 10 m s^{-1}) and q (heavy gray lines, contours at 0.15, 0.3, 0.6 PVU), and (c) $w - w_{sg}$ (contour interval 0.2 cm s^{-1}). Only the central 1800 km of the computational domain is shown.

those of waves emitted by the shear front and different vertical structure, consistent with wave propagation through the two distinct cross-front flows.

We note that there are certain similarities, particularly in θ and v, between this steady-state front and the postcollapse SG solutions of Cullen and Purser (1984) and Koshyk and Cho (1992). In both θ (Fig. 7a) and v (Fig. 7b), a region of intense gradients (i.e., the front) extends upward from the surface and separates broad gradients on the cold side of the front from much weaker gradients on the warm side. Without a more detailed comparison, however, it is not clear that these discontinuous SG solutions would be obtained in the limit of zero horizontal diffusion.

5. Analysis

The foregoing numerical simulations indicate that, near and following frontal collapse, small but significant deviations from SG are present. Prior to collapse, the deviations from SG for the shear front appear to include both gravity waves and higher-order corrections to SG, while the deformation-front simulations contain gravity waves associated with either the model initialization or with time variations of α, which may mask other deviations from SG. In postcollapse solutions with diffusion, gravity waves appear to account for most of the differences from SG (at least in the secondary circulation); since spurious gravity wave sources have been eliminated in these solutions, the waves must be emitted by the frontogenesis.

In this section, we scale the PE and look explicitly at how deviations from the SG solutions arise as either inertia–gravity waves or higher-order balanced corrections. We derive certain scaling properties of the higher-order corrections and use these to demonstrate more conclusively that gravity waves dominate the corrections to the SG crossfront circulation in the case of the "steady-state" deformation front. Although we do not provide a comprehensive analysis of the wave emission, we will discuss some parameter dependencies of both the corrections and the emitted waves.

a. Frontal scaling and the SG equations

Following Hoskins and Bretherton (1972), we introduce separate scales for the cross- and alongfront velocities and nondimensionalize (1) using

$$
\left.
\begin{aligned}
&x \sim l, && z \sim h, \\
&v \sim V, && u \sim U = \epsilon V, \quad w \sim hU/l = \delta\epsilon V, \\
&t^{-1} \sim U/l = \text{Ro}\epsilon f, && \phi \sim flV, \quad \theta \sim \theta_0 flV/gh.
\end{aligned}
\right\}
$$

(9)

Three parameters have been introduced in (9): the frontal parameter, $\epsilon = U/V$; the aspect ratio, $\delta = h/l$; and the Rossby number, $\text{Ro} = V/fl$. Typically, fronts are characterized by $\epsilon \ll 1$ and $\text{Ro} \geq O(1)$.

The scalings may be refined by relating h to l, and U to V, as in the SG solutions. In geostrophic coordinates, the vertical scale of the SG solution is the Rossby depth, $fL/\tilde{N}$, where L is the horizontal scale and $\tilde{N}^2 = (g\rho_0/f\theta_0)q$ (e.g., see Hoskins and Bretherton 1972). An identical relation of length and height scales holds in physical coordinates, since the SG solution satisfies, for example, $v_x/v_z = v_X/v_Z$. For our purposes, the background buoyancy frequency N adequately approximates $\tilde{N}$ and we choose

$$h = fl/N, \quad \delta = f/N.$$

To relate U and V, note that the Sawyer–Eliassen equation (5) suggests that fu_x should be of magnitude comparable to αv_x for the deformation front, and to Λv_z for the shear front. Hence, for the deformation front,

$$U = (\alpha/f)V, \quad \epsilon = \alpha/f;$$

and for the shear front,

$$U = (\Lambda/N)V, \quad \epsilon = \Lambda/N.$$

Neglecting nonhydrostatic and compressible terms, the nondimensionalizations (9) applied to (2) yield

$$\epsilon^2\left(\text{Ro}\frac{du}{dt} + \mathbf{v}\cdot\nabla\bar{u}\right) - v = -\phi_x + \epsilon^2 E u_{xx}, \quad (10a)$$

$$\text{Ro}\frac{dv}{dt} + \mathbf{v}\cdot\nabla\bar{v} + u = E v_{xx}, \quad (10b)$$

$$\theta - \phi_z = 0, \quad (10c)$$

$$\text{Ro}\frac{d\theta}{dt} + \mathbf{v}\cdot\nabla\bar{\theta} = E\theta_{xx}, \quad (10d)$$

$$u_x + w_z = 0, \quad (10e)$$

where $E = \nu/(\epsilon fl^2)$, and $d/dt = \partial_t + (\text{Ro}^{-1}\bar{u} + u)\partial_x + w\partial_z$. The nondimensional background variables ($\bar{u}$, $\bar{v}$, $\bar{\theta}$) are given by ($-x$, y, z) for the deformation front, and (z, 0, $-y + z$) for the shear front.

When $\epsilon \ll 1$ and $\text{Ro} = O(1)$, the natural approximation to (10) is to neglect terms proportional to ϵ^2 in (10a), while retaining (10b–e). The resulting equations are the SG equations, modified by horizontal diffusion.

The approximation of cross-front geostrophic balance introduces errors that are $O(\epsilon^2\text{Ro}, \epsilon^2 E)$. As noted in the Introduction, these errors increase near collapse, since l shrinks and both Ro and E grow (thinking of l as the instantaneous cross-front scale), while ϵ is constant. If the cross-front scale shrinks to the point that $\epsilon^2\text{Ro} \sim 1$, the cross-front acceleration can not be neglected in (10a) and SG is formally invalid.

The numerical solutions indicate that diffusion selects the minimum l and prevents collapse. Similarly, (10b) and (10d) predict that, when $\nu \neq 0$, $E \sim \text{Ro}$ and diffusion balances advection near collapse, since

both Ro and E become large. The minimum scale is then $l \sim \nu/\epsilon V$, while the maximum Ro $\sim \epsilon V^2/f\nu$.

Table 1 lists the values of nondimensional parameters for four of the numerical simulations and compares scaling estimates for u, u_x, and du/dt with values obtained directly from the model output. In agreement with the numerical results, all the simulations except that of the postcollapse Eady wave are in regimes where the corrections to SG should be small (i.e., ϵ^2 Ro is small). In fact, because of the tendency for the front to form where $u \approx 0$, ϵ^2 Ro overestimates du/dt, so that cross-front geostrophic balance (and SG) is a reasonable first approximation even for the postcollapse shear front. The estimates for u and u_x are also encouragingly accurate.

Because the scaling overestimates the cross-front advections, the solutions with diffusion have $E \ll$ Ro, rather than $E \sim$ Ro. The simulations do, however, confirm the linear dependence of l on ν predicted by the scaling. For example, if the diffusion in the shear-front simulations is varied, the maximum vertical vorticity at a given time varies linearly with ν^{-1}.

b. Higher-order corrections to SG

The next-order corrections to SG can be obtained by writing

$$v = v_{sg} + \epsilon^2 v' + O(\epsilon^4),$$

$$u = u_{sg} + \epsilon^2 u' + O(\epsilon^4), \quad \text{etc.,} \quad (11)$$

where the subscript sg now denotes a solution of the prognostic SG equations [i.e., (10) with $O(\epsilon^2)$ terms neglected]. Substituting (11) into (10) yields, at $O(\epsilon^2)$,

$$v' - \phi'_x = F_{sg}, \quad (12a)$$

$$\text{Ro}\,d_{sg}v' + \mathbf{v}' \cdot \nabla(\bar{v} + \text{Ro}v_{sg}) + u' - Ev'_{xx} = 0, \quad (12b)$$

$$\theta' - \phi'_z = 0, \quad (12c)$$

$$\text{Ro}\,d_{sg}\theta' + \mathbf{v}' \cdot \nabla(\bar{\theta} + \text{Ro}\theta_{sg}) - E\theta'_{xx} = 0, \quad (12d)$$

$$u'_x + w'_z = 0, \quad (12e)$$

where $F_{sg} \equiv \text{Ro}\,d_{sg}u_{sg} + \mathbf{v}_{sg} \cdot \nabla\bar{u} - Eu_{sgxx}$, and $d_{sg} \equiv \partial_t + (\bar{u} + u_{sg})\partial_x + w_{sg}\partial_z$. While (12a–e) are prognostic equations for the primed variables, a similar expansion in powers of ϵ^2 can be used to extend to higher orders our technique for diagnosing the SG solution from the model PV.

The SG solution forces the next-order corrections via F_{sg}, which consists of the cross-front acceleration and diffusion neglected by SG. Unlike the SG solution, the corrections include an ageostrophic contribution to the alongfront wind, since F_{sg} appears in (12a). Equations (12) are otherwise dynamically similar to SG; they retain the (linearized) material derivatives of v' and θ' while neglecting du'/dt, and thus do not support internal gravity waves. Because they are forced by terms neglected by SG, the next-order corrections are $O(\epsilon^2$ Ro, $\epsilon^2 E)$ compared to the SG solution.

The higher-order corrections to SG have a dependence on the basic-state parameters that can be used to distinguish them from gravity waves. For fixed E, the SG equations and (12) are independent of ϵ. Varying α or Λ (with E fixed) thus does not change the spatial structure of either the SG solution or the higher-order corrections, but simply rescales time and the magnitude of the cross-front circulation. In contrast, the spatial structure of gravity waves embedded in the frontal flow is sensitive to α, as shown in Figs. 2 and 3 and discussed in section 3.

We have repeated the simulation of the steady-state deformation front (section 5b, Fig. 7) using $\alpha = 0.1f$ and $\nu = 0.5 \times 10^5$ m^2 s^{-1}. Results are shown in Fig. 8 (E is unchanged from the previous case with $\alpha = 0.2f$ and $\nu = 10^5$ m^2 s^{-1}, since both α and ν have been halved). Comparison of Fig. 8a with Fig. 7a shows that, as predicted by the nondimensional form of the SG equations, θ is nearly identical in the two solutions. The structure of $w - w_{sg}$, however, changes fundamentally (Fig. 8b). The primary features of the $\alpha = 0.2f$ case, which have the structure of standing waves of wavelength $2H$ above the frontal nose, are not present when $\alpha = 0.1f$. Instead, above the surface front $w - w_{sg}$ consists of an updraft sloping away from the

TABLE 1. Various dimensional and nondimensional parameters for different simulations, and comparison of scaling estimates with quantities obtained directly from the simulations. Values are calculated as follows: V is the maximum of $|v|$ over the computational domain; Ro is the ratio of the maximum vertical vorticity to f; $l = V/(f\text{Ro})$; ϵ is given by the estimates preceding (10); $E = \nu/(\epsilon f l^2)$; and u, u_x, and du/dt denote the maximum values of those quantities in the simulations. Note that ϵ is the scaling estimate for u/V, ϵRo is the estimate for u_x/f, and ϵ^2 Ro is the estimate for the ratio of du/dt to fV.

Case	V (m s^{-1})	Ro	l (km)	ϵ	u/V	E	ϵRo	u_x/f	ϵ^2Ro	$\dfrac{du}{dt}\Big/fV$
G89, $\nu = 0$, 16 h	32	3.0	106	0.2	0.28	0.	0.6	0.9	0.12	0.05
Eady, $\nu = 0$, day 8	45	2.6	173	0.3	0.24	0.	0.78	0.39	0.23	0.06
G89, $\nu = 10^5$ m^2 s^{-1}, steady state	38	4.2	90	0.2	0.26	0.62	0.84	1.1	0.17	0.08
Eady, $\nu = 10^5$ m^2 s^{-1}, day 9	90	24	38	0.3	0.24	2.3	7.2	3.4	2.2	0.3

(a) w, $\vartheta + \bar{\vartheta}$ at 96 h (β=3.46)
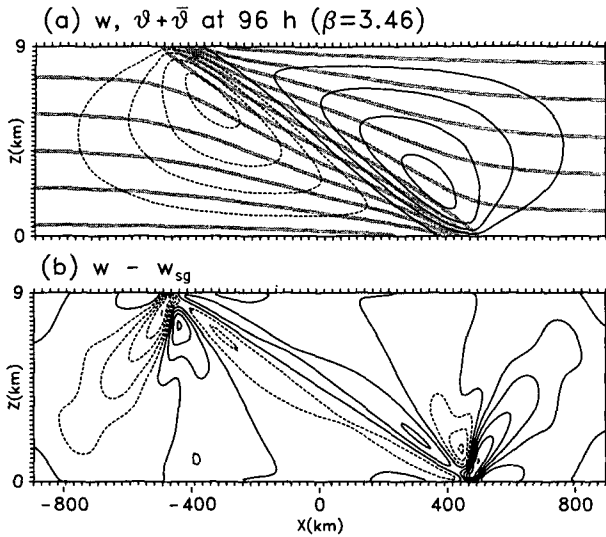

(b) w - w_{sg}

FIG. 8. Deformation front, with parameters as in Fig. 7 except α = 0.1f, at 96 h (β = 3.46): (a) w (contour interval 0.5 cm s^{-1}) and θ (heavy gray lines, contour interval 2 K) and (b) $w - w_{sg}$ (contour interval 0.02 cm s^{-1}).

front, a downdraft oriented vertically above the frontal nose, and, finally, an updraft–downdraft couplet sloping along the frontal surface.[3]

Since the structure of these features changes as α varies, $w - w_{sg}$ is not, as conjectured by G89, associated mainly with higher-order corrections to SG, but must contain significant gravity waves. When $\alpha = 0.2f$, the structure of $w - w_{sg}$ is consistent with a stationary gravity wave, indicating that gravity waves dominate the higher-order corrections. When $\alpha = 0.1f$, the gravity wave signal in $w - w_{sg}$ is less distinct; in this case, stationary waves should have vertical wavelengths of somewhat less than 4H above the frontal nose, decreasing to 2H at the edge of the domain shown in Fig. 8. Thus, it is likely that both higher-order corrections and waves are present when $\alpha = 0.1f$, as was the case for the precollapse Eady wave.

Although at best they explain only a portion of the differences between the model and SG cross-front circulations, the next-order corrections to SG approximate the ageostrophic alongfront wind, v_a, reasonably. Returning to the steady-state deformation front with $\alpha = 0.2f$, Fig. 9 compares the model v_a with that predicted by (12a). In contrast to $w - w_{sg}$, which for this front is associated almost exclusively with gravity waves (Fig. 7c), v_a is clearly dominated by the next-order correction to SG. In v_a, gravity waves appear as rela-

tively small deviations from the *corrections* to SG, as shown by the difference between v_a and that predicted by the corrections (Fig. 9c). The agreement between v_a and (12a) diminishes for the postcollapse Eady wave, although (12a) still predicts the correct sign and magnitude for v_a.

c. Gravity wave generation and propagation

By formally expanding the PE in powers of ϵ^2, one could, in principle, produce successively higher-order corrections to SG. Such a series solution, however, can not describe freely propagating gravity waves and need be only asymptotically valid. Alternatively, linear equations governing *any* small deviations away from SG can be obtained by subtracting the SG equations from the full PE and neglecting terms that are quadratic in the deviations. Letting primes denote the deviations, the resulting equations are identical to (12) except that (12a) is replaced by

$$\epsilon^2[\mathrm{Ro}\, d_{sg} u' + \mathbf{v}' \cdot \nabla(\bar{u} + u_{sg}) - E u'_{xx}]$$
$$- v' + \phi'_x = -F_{sg}. \quad (13)$$

No profound progress has been made; these are the hydrostatic PE, linearized about the known (approx-
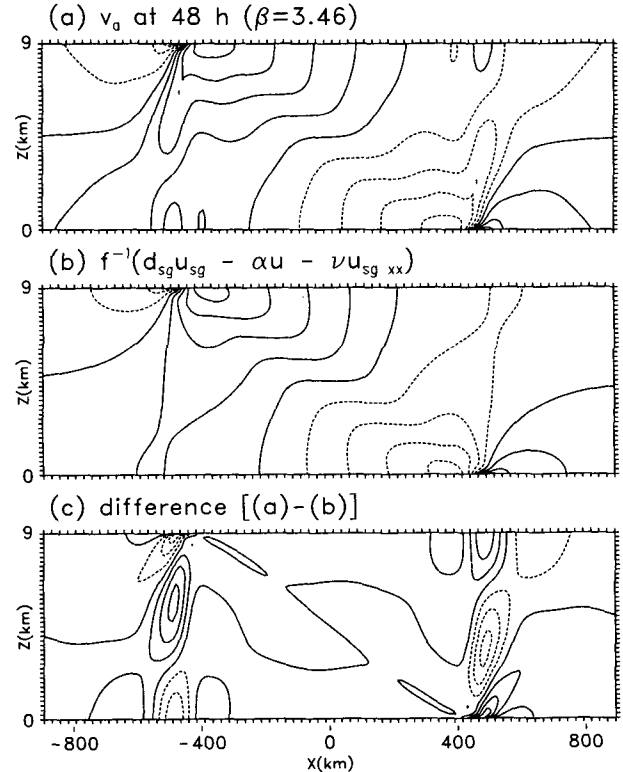
(a) v_a at 48 h (β=3.46)

(b) $f^{-1}(d_{sg}u_{sg} - \alpha u - \nu u_{sg\,xx})$

(c) difference [(a)-(b)]

FIG. 9. As in Fig. 7 but (a) v_a (contour interval 0.4 m s^{-1}), (b) the ageostrophic v predicted by (12a) (contour interval 0.4 m s^{-1}), and (c) the difference of the two fields (contour interval 0.2 m s^{-1}).

---

[3] As noted previously for Fig. 2c, the updraft–downdraft couplet depends on the grid spacing and is a result of truncation errors. The other primary features in $w - w_{sg}$ persist at higher resolutions.

imate) SG solution and forced by F_{sg}.[4] By linearizing, we neglect any modification of the frontogenesis by the deviations.

Understanding the differences between the PE and SG solutions now amounts to determining the linear response to the forcing F_{sg}. Clearly, internal waves, inertial oscillations, and "balanced" perturbations (i.e., the higher-order corrections to SG) are all possible components of the response. Their relative magnitudes will depend on the temporal and spatial scales of the SG solution, through both the forcing and the coefficients of (12b–e) and (13).

First, we note that the gravity wave response to the forcing will be significant only at spatial and temporal scales that are comparable to or longer than those of F_{sg}, since shorter waves will be subject to destructive interference. Nondimensionalizing with (7), the waves must therefore have k, m, $\tilde{\omega} \leq O(1)$, where k and m are the horizontal and vertical wavenumbers, respectively, and $\tilde{\omega} = \omega - k(\bar{u} + u_{sg}) - mw_{sg}$ is the intrinsic frequency.

Next, consider the requirements for the existence of inertia–gravity waves. Their dispersion relation is

$$\epsilon^2 \, \mathrm{Ro}^2 \tilde{\omega}^2 = \frac{m^2 + k^2}{m^2 + \delta^2 k^2}, \qquad (14)$$

assuming that the flow is slowly varying and, for simplicity, ignoring variations in the local buoyancy frequency. (Both conditions are qualitatively applicable away from the frontal zone.) By (14), waves with $\tilde{\omega} \leq O(1)$ can propagate only if $\epsilon \, \mathrm{Ro} \geq O(1)$, which in terms of dimensional quantities is the familiar requirement that the waves' frequency relative to the flow is greater than f.

Thus, as frontogenesis proceeds, l will shrink, Ro will increase, and the flow will pass from a regime in which $\epsilon \, \mathrm{Ro} \ll 1$ and there is little gravity wave response to F_{sg}, into a regime in which $\epsilon \, \mathrm{Ro} \geq O(1)$ and significant gravity waves are emitted by the front. Initially, the emitted waves share the dominant scales of F_{sg}, since (14) can be satisfied with k, m, $\tilde{\omega} \sim 1$ for $\epsilon \, \mathrm{Ro} \sim 1$. When $\epsilon \, \mathrm{Ro} \gg 1$, (14) requires that $m \sim \epsilon^{-1} \mathrm{Ro}^{-1} \ll 1$, so that the waves will have a longer vertical scale than the SG solution. In either case the waves are hydrostatic, unless the front is narrow enough that $\epsilon \, \mathrm{Ro} \sim \delta^{-1}$.

---

[4] In the interest of brevity, we have so far ignored vertical accelerations, which are retained by the numerical model but are neglected by SG. Formally, the vertical acceleration is $O(\delta^2) = O(f^2/N^2)$ compared to the cross-front acceleration. Forcing in the vertical momentum equation, however, could conceivably be much more efficient in generating gravity waves than a source of horizontal momentum. To test this possibility, the simulations of the postcollapse Eady wave have been repeated using a hydrostatic model (J. Whitaker 1992, personal communication). The hydrostatic simulations are essentially indistinguishable from those using the full model.

Results for the inviscid Eady wave agree qualitatively with this analysis. By day 8, the front has contracted sufficiently that $\epsilon \, \mathrm{Ro} = 0.84$ (Table 1) and a suggestion of gravity wave activity appears in w and $w - w_{sg}$ (Fig. 5). However, collapse occurs within 4 h, effectively ending the inviscid integration, and it is unclear whether gravity wave amplitudes would continue to increase as the frontal scale shrank. The simulations of the deformation front with $\alpha = 0.2f$ also have $\epsilon \, \mathrm{Ro} \sim 1$ as the front nears collapse, but the waves associated with the model initialization or time variation of α mask any weak waves emitted by the front.

The presence of horizontal diffusion has several implications for gravity wave emission. As discussed above, diffusion determines l and hence the spatial scales of F_{sg} and the emitted gravity waves. In addition, the diffusion alters the local time scale of the SG solution, since it balances the cross-front advections near the front, so that the local time derivative becomes relatively small. (The smallness of the time derivative is supported by a term-by-term diagnosis of the v and θ equations for the Eady wave solutions following collapse.) The local frontal structure is then approximately fixed, F_{sg} changes slowly on the local advective time scale, and waves generated in the postcollapse, diffusive solutions should be nearly stationary, with $\omega \ll 1$. Finally, diffusion also damps the wave motions substantially; for $\nu = 10^5 \, \mathrm{m}^2 \, \mathrm{s}^{-1}$, waves of 100-km horizontal wavelength have e-folding times of about 40 minutes.

These predictions hold qualitatively for the postcollapse shear front and the steady-state deformation front. Horizontal wavelengths for the waves (Figs. 6, 7) are roughly 100–200 km, which is broadly consistent with $l \leq 100$ km (Table 1), and the waves are nearly stationary, though in the former case their structure changes gradually as the Eady wave evolves. As shown in Table 1, both solutions also appear to be in the correct regime for wave generation, since they have $\epsilon \, \mathrm{Ro} \geq O(1)$. Furthermore, the Eady wave at day 9, which exhibits the gravity waves of largest amplitude, has the largest magnitude of F_{sg} (as measured by $\epsilon^2 \, \mathrm{Ro}$).

It might be anticipated that wave amplitudes could be estimated [in a manner similar to that of Spall and McWilliams (1992)] by balancing F_{sg} against terms associated with gravity wave propagation, such as $\epsilon^2 \, \mathrm{Ro} \, d_{sg} u'$ in (13). As was illustrated in Fig. 9, however, the primary balance in the model solutions is between F_{sg} and $v_a = v' - \phi'_x$ for the parameter regime considered here. In essence, although F_{sg} contains scales that can force inertia–gravity waves, most of the response is at scales that are balanced or nonpropagating.

While gravity waves are not the primary corrections to SG in v, they account for most of the deviations from SG in u and w. This can occur because the gravity wave fields need not obey the scaling assumption that, for dimensional variables, $u' \ll v'$. Thus, since higher-order corrections to SG do satisfy $u' \ll v'$, the gravity

waves can account for most of $u - u_{sg}$, but still be a small correction to v_a.

Our approach to understanding wave emission is similar to that of Ley and Peltier (1978). They also subtracted the SG equations from the PE to obtain equations for the deviations from SG, which were forced by the terms neglected by SG. Their analytical solutions assume that the waves propagate through a uniform medium and that dissipative processes suddenly turn off the wave forcing prior to collapse (leading to a pulse of propagating waves). In contrast, our results emphasize that variations in the frontal flow control the wave propagation, and we find that horizontal diffusion results in wave forcing that is nearly steady on the wave time scale.

Wave emission has been approximated as the linear response to specified forcing in other fluid-dynamical contexts. These include the aerodynamic generation of sound (Lighthill 1952) and the slow manifold problem in large-scale atmospheric dynamics (e.g., Lorenz and Krishnamurty 1987).

6. High-resolution simulations

a. The deformation front revisited

The simulations with diffusion demonstrate that frontogenesis can generate gravity waves once a front becomes sufficiently intense. However, none of the solutions to this point have contained counterparts of either the stationary waves extending back along the frontal surface or the trapped, resonant waves beneath the frontal surface found by GWC. It is possible that the resolution used in our simulations, which is poorer than that used by GWC, is too coarse to capture the emission of such waves.

As a first step toward resolving this issue, we have repeated the inviscid deformation front simulation of section 3b using horizontal and vertical grid intervals of 3.1 km and 28.1 m, respectively. As in section 3b, the variable deformation rate $\alpha(t)$ is given by (8) with $\alpha_f = 0.1f$ and $\tau = 1$ d. The horizontal resolution and final deformation rate are comparable to those used by GWC, while the cross-front temperature contrast and background N^2 are smaller by factors of 1.8 and 3.5, respectively.

Figure 10 shows w and θ when the integrated deformation $\beta = 1.15$, along with a close-up view of w and PV near the surface front. As noted in section 3, SG frontal collapse in this case occurs when $\beta = 1.2$, or roughly 1.5 h after the time shown in Fig. 10. The solution is smooth and close to the SG solution (not shown) at this time, except for some small-amplitude ripples in w. Although these ripples are nearly stationary and extend vertically above the surface front, their location and structure resemble those of the gravity waves present in the other deformation-front solutions
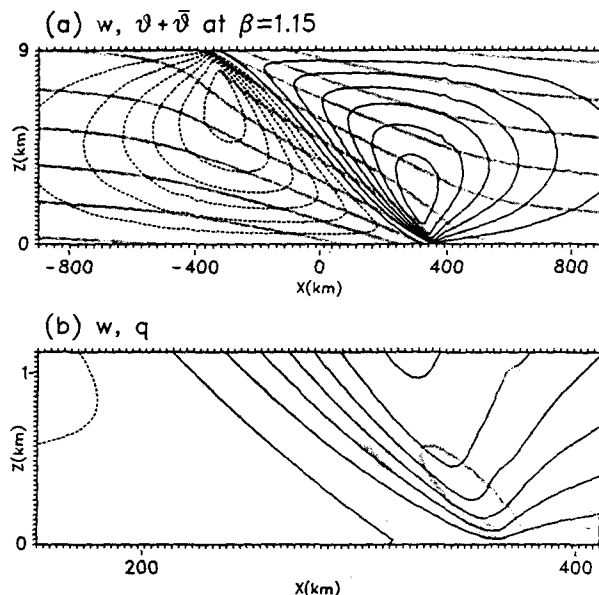

(a) w, $\vartheta + \bar{\vartheta}$ at $\beta = 1.15$

(b) w, q

FIG. 10. Inviscid deformation front (as in Fig. 4b) at high resolution: (a) w (contour interval 0.25 cm s^{-1}) and θ (heavy gray lines, contour interval 2 K) and (b) detail of frontal structure showing w [as in (a)] and the anomaly q (heavy gray lines, contours at 0.01, 0.04, 0.1 PVU). Tick marks are shown every 8 grid points in (a), and every grid point in (b).

(both those generated by the time variation of α and those emitted by the steady-state fronts) rather than the GWC waves. Furthermore, no hint of waviness is present in the cold air directly beneath the surface front. As at lower resolution, then, there are no large differences from the smooth SG solution, nor are there obvious counterparts to the waves found by GWC.

Before continuing our search for the GWC waves, we note that, while the model fields appear to be sufficiently resolved (such as w in Fig. 10b), truncation errors are significant by this time. The size of the numerical errors is evident in the PV anomalies near the frontal nose, which have magnitudes comparable to the initial, uniform PV (Fig. 10b). As in the solutions with explicit diffusion, a positive anomaly extends upward along the frontal surface, but the numerical errors have also produced a smaller negative anomaly on the cold side of the surface front.

In agreement with inviscid simulations at lower resolution, the PV generation begins just prior to SG frontal collapse (i.e., $\beta = 1.2$). Table 2 further illustrates this point by listing the maximum PV anomalies at various times and for simulations with various resolutions. At $\beta = 1.07$, the halving of the maximum anomalies with doubling of the resolution indicates that the numerical solutions are converging, with increasing resolution, toward uniform PV. When $\beta = 1.18$, the magnitude of the PV anomalies has grown to 0.3 PVU, or three times the initial PV, and does not decrease

TABLE 2. The maximum PV anomaly (10^{-1} PVU) at various integrated deformations (β) and for different horizontal resolutions (Δx), for the deformation front stimulations described in the text. Frontal collapse is predicted by SG at $\beta = 1.20$. $\Delta z/\Delta x$ is fixed at 0.01 as Δx varies.

Δx (km)	β			
	0.860	0.976	1.17	1.18
25.0	0.17	0.36	0.75	3.4
12.5	0.09	0.26	0.78	3.0
6.1	0.03	0.12	0.65	4.5
3.1	>0.01	0.04	0.30	4.0

with increased resolution. The collapse of the model fields to the grid scale thus appears to approach the time of SG frontal collapse as the resolution increases. In addition, the onset of spurious PV generation in the model is a sensitive indicator of incipient collapse and the associated poor resolution.

b. Simulations following GWC

Since the GWC waves are not present in our deformation-front simulations even at 3-km horizontal resolution, we now turn to the specific case examined by GWC.

We consider the same physical problem as GWC, except we use a time-variable deformation rate and a different initialization for the cross-front circulation. Specifically, the initial θ is given by Eq. (1) in GWC and the initial ϕ and v are calculated from the hydrostatic and geostrophic relations. Again, $\alpha(t)$ is given by (8) with $\alpha = 0.1 f$ and $\tau = 1$ d, and the initialization consists of setting u and w to be zero at the initial time. Though we find that the GWC initialization (in which u and w are diagnosed from the quasigeostrophic w equation) produces much stronger gravity waves, the presence or absence of these initialization waves changes the results that follow only cosmetically. For now, the model resolution is chosen to agree with experiment 3 of GWC, with horizontal and vertical grid intervals of 5 km and 322 m, respectively.

The GWC simulations have no explicit dissipation and exhibit stationary waves above the front beginning when $\beta = 1.22$ (i.e., after ~34 h at $\alpha = 0.1 f$) and continuing through $\beta = 1.5$ (~42 h). In contrast, in our attempts to replicate these inviscid simulations spurious PV production begins before $\beta = 1.1$ and the solutions are overwhelmed by computational noise throughout the period $1.2 \leqslant \beta \leqslant 1.5$. Presumably, the generation of PV once again signals the onset of frontal collapse near $\beta = 1.1$; the noisy solutions that follow are consistent with this. Thus, it is likely that the inviscid solutions of GWC continue nearly 12 h beyond frontal collapse, contrary to the conclusions of Gall et al. (1987), who suggest that collapse occurs for $\beta \approx 1.5$.

To reach the regime where GWC find waves ($\beta \geqslant 1.2$) and maintain a well-resolved solution, we include horizontal diffusion with $\nu = 0.5 \times 10^4$ m^2 s^{-1} beginning at $\beta = 1.0$.

The vertical velocity from our "reproduction" of the GWC simulation is shown in Fig. 11a for $\beta = 1.4$ and should be compared with the upper-right panel of Fig. 3 in GWC. As in GWC, there are upward-propagating (standing) gravity waves above (below) the surface front. In fact, the solution reproduces the structure of w found by GWC in surprising detail: five distinct maxima appear just above the surface front (although the weakest cannot be seen in Fig. 11a because of the coarse contour interval of 0.4 cm s^{-1}) and the minimum w in the standing waves beneath the front is roughly 0.4 cm s^{-1}.

While the solution shown in Fig. 11a clearly captures the generation of the GWC waves, our previous simulations of the deformation front, which were in most ways similar, clearly lack the GWC waves. Compared to GWC, however, those previous simulations used relatively finer vertical resolution for a given horizontal resolution. The GWC simulation considered here, for example, has a vertical grid interval that is roughly $1/16$ of the horizontal, while our other deformation-front simulations of section 3 use $\Delta z \sim \Delta x / 100$.

The importance of the vertical resolution may be determined by repeating the GWC simulation using a smaller grid spacing in the vertical. For convenience,
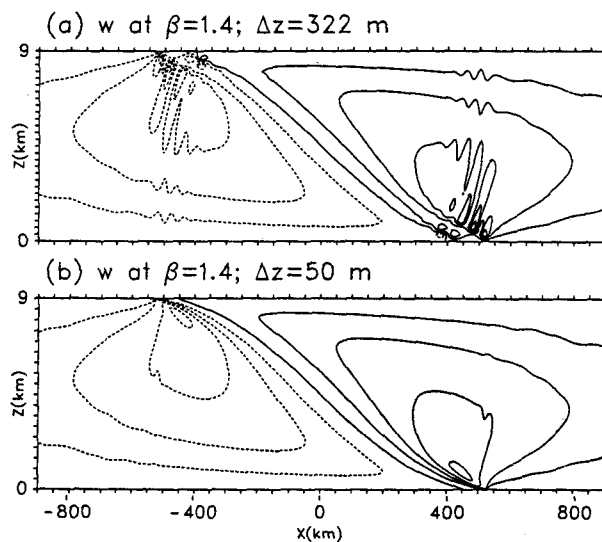

FIG. 11. w for deformation-front simulations using (a) coarse vertical resolution ($\Delta z = 322$ m), and (b) fine vertical resolution ($\Delta z = 50$ m). The simulations are otherwise identical and are comparable with those of GWC, except, as discussed in the text, for the use of horizontal diffusion and $\alpha(t)$ given by (8). The contour interval is 0.4 cm s^{-1}; tick marks on the horizontal axis appear every 10 grid points in (a) and (b), while ticks on the vertical axis appear every grid point in (a) and every 10 grid points in (b).

we choose $\Delta z = 50$ m $= \Delta x / 100$. Figure 11b, which shows w for this simulation, demonstrates that the solution changes dramatically as the vertical resolution increases; w returns to the generally smooth structure found in the previous deformation fronts (e.g. Fig. 10) and also exhibits much smaller vertical scales near the boundaries than at the coarser vertical resolution. Although there are weak ripples in w above the frontal nose, the GWC waves have vanished.

The inevitable conclusion is that the GWC solutions have insufficient vertical resolution and that truncation errors are in large part responsible for the gravity waves in those solutions. This occurs because the aspect ratio of the computational grid is large compared to that of the frontal flow, which is $O(f/N)$, so that, as the front collapses, solution becomes poorly resolved in the vertical first. Equivalently, for the grid aspect ratio chosen by GWC, some well-resolved horizontal scales correspond to vertical scales that are poorly resolved, and hence the numerical solution contains little physical information at those horizontal scales, as discussed in more general terms by Lindzen and Fox-Rabinovitz (1989). Although the horizontal wavelength of the GWC waves ($\sim$40 km) is well resolved, the probable importance of vertical truncation errors is evident in the $2\Delta z$ vertical wavelength of the standing waves beneath the front and in the decreased vertical scales of the solution at higher vertical resolution.

The notion that insufficient resolution in numerical simulations might lead to spurious gravity wave production has been discussed previously by Pecnick and Keyser (1989) and Persson and Warner (1991), who examined cases of upper-level frontogenesis and conditional symmetric instability, respectively. Spurious gravity waves, possibly linked with poor resolution of frontogenesis, have also been noted by Volkert and Bishop (1990) and Tremblay (1992).

7. Summary and discussion

In numerical simulations of both inviscid frontogenesis prior to frontal collapse and postcollapse frontogenesis with horizontal diffusion, we find, as have others, that SG solutions generally provide good approximations to the overall structure of the front and the timing of frontal collapse. Careful examination of the differences from SG noted in previous studies reveals that the "split updraft" found by G89 is produced by propagating gravity waves associated with the model initialization, while the stationary waves found by GWC are numerical artifacts produced by insufficient vertical resolution.

Nevertheless, important deviations from SG exist and can have magnitudes comparable to the SG solution in extreme cases. In the cross-front circulation, gravity waves account for the largest deviations; even if such spurious sources as the model initialization or

insufficient resolution are eliminated, gravity waves are emitted when the frontogenesis is sufficiently intense. Adjustment to time variations in the background deformation or shear can also give rise to internal waves. Speculation (G89) that higher-order corrections to SG should dominate gravity waves is thus incorrect in the cases examined here, although when deviations from SG are small (such as in the precollapse Eady wave or the steady-state deformation front with $\alpha = 0.1 f$), there are indications that the waves and higher-order corrections have comparable magnitudes. The next-order corrections to SG also provide a good approximation to the alongfront ageostrophic wind.

Since numerical simulations of inviscid frontogenesis rapidly become poorly resolved, we include horizontal diffusion to extend the numerical solutions beyond frontal collapse. The diffusion limits the contraction of the front and produces strong positive PV anomalies along the frontal surface. The emitted waves in this case are stationary above the nose of the surface front and result in a low-level maximum in w that is not present in the SG solutions.

Our analysis of the gravity wave emission builds on the ideas of Ley and Peltier (1978). We reduce the problem of weak emission to the calculation of the linear forced gravity wave field within a spatially and temporally varying medium, where the SG solution defines both the medium and, through the cross-front acceleration, the forcing. The dispersion relation for inertia–gravity waves then indicates that, consistent with the numerical solutions, emission should become significant while SG is still formally valid, when the advective time scale becomes comparable to (and, preferably, somewhat smaller than) f^{-1}. Furthermore, consideration of the wave forcing in the presence of diffusion predicts that the emitted waves will be stationary, again consistent with the numerical solutions.

Although the basic dynamics of wave emission do not depend on dissipation, the horizontal wavelength of the emitted waves depends strongly on the magnitude of the diffusion, which determines the minimum scale of the front and hence of the forcing for the gravity waves. However, certain properties of the emitted waves are insensitive to the magnitude and form of the dissipation: the waves will be hydrostatic for a broad range of diffusion, and the waves will be nearly stationary with respect to the front as long as the dissipation acts to balance the frontogenesis and produce a locally fixed frontal structure.

Because of the magnitude of the diffusion, the scale of the front remains large enough that cross-front geostrophic balance is a good approximation in all the cases examined, except perhaps for the postcollapse Eady wave, and the wave emission is thus usually a minor correction to SG. Relatedly, we have not considered how the emitted waves might feed back on the SG solution, although this feedback may again be im-

portant in the case of the postcollapse Eady wave. An associated question is the existence of a frontal singularity in the inviscid PE. Our results suggest that theories of frontogenesis very near collapse must consider the possible role of wave emission. A computationally attractive approach to this question is to degrade the cross-front geostrophic balance by increasing α or Λ and so increasing the frontogenetical forcing.

While the idealized two-dimensional problems examined here are ideal for illuminating the basic dynamics of the frontogenesis and wave emission, several additional processes will be of practical importance. First, nonadiabatic processes are important in real fronts. The inclusion of moisture and latent heat release would intensify the cross-front circulation and enhance the wave emission. Similarly, more realistic treatments of the lower boundary, such as applying a surface drag, will inhibit the cross-front geostrophic balance at low levels, again potentially enhancing the wave emission.

In addition, alongfront variability and curvature can be expected to modify the gravity wave emission. Alongfront propagation and dispersion of emitted waves will quantitatively change the pattern of emitted gravity waves. More important effects result from the possibility of alongfront instabilities that will alter the mature frontal structure and may provide a brake on frontogenesis. Frontal instabilities will change the gravity wave forcing by the frontogenesis, both by dramatically increasing the cross-front accelerations and by introducing relatively high frequencies, which will allow waves that propagate relative to the front. Although instabilities may control the frontal structure near collapse, we note that wave emission can occur at the same time or even earlier in the frontal development, since instabilities are expected when the Richardson number $Ri = Ro^{-1} \ll 1$, while emission requires $Ro^{-1} \sim \epsilon$.

Acknowledgments. Dr. S. T. Garner provided a thorough and helpful review.

REFERENCES

Blumen, W., 1992: A semigeostrophic Eady wave frontal model incorporating momentum diffusion. Part III: Wave dispersion and dissipation. *J. Atmos. Sci.,* **49,** 1061–1074.

Chan, S. T. D., and H. R. Cho, 1989: Meso-β-scale potential vorticity anomalies and rainbands. Part I: Adiabatic dynamics of potential vorticity anomalies. *J. Atmos. Sci.,* **46,** 1713–1723.

Cullen, M. J. P., and R. J. Purser, 1984: An extended Lagrangian theory of semigeostrophic frontogenesis. *J. Atmos. Sci.,* **41,** 1477–1497.

Davies, H. C., and J. C. Müller, 1988: Detailed description of deformation-induced semigeostrophic frontogenesis. *Quart. J. Roy. Meteor. Soc.,* **114,** 1201–1220.

Eliassen, A., 1962: On the vertical circulation in frontal zones. *Geophys. Publ.,* **24,** 147–160.

Gall, R. L., R. T. Williams, and T. L. Clark, 1987: On the minimum scale of fronts. *J. Atmos. Sci.,* **44,** 2562–2574.

——, ——, and ——, 1988: Gravity waves generated during frontogenesis. *J. Atmos. Sci.,* **45,** 2205–2219.

Garner, S. T., 1989: Fully Lagrangian numerical solutions of unbalanced frontogenesis and frontal collapse. *J. Atmos. Sci.,* **46,** 717–739.

Hoskins, B. J., and F. P. Bretherton, 1972: Atmospheric frontogenesis models: Mathematical formulation and solution. *J. Atmos. Sci.,* **29,** 11–37.

Jones, W. L., 1969: Ray tracing for internal gravity waves. *J. Geophys. Res.,* **74,** 2028–2033.

Klemp, J. B., and R. B. Wilhelmson, 1978: The simulation of three-dimensional convective storm dynamics. *J. Atmos. Sci.,* **35,** 1070–1096.

Koclas, P., A. Staniforth, and H. Warn, 1986: A variable-resolution finite-element model of frontogenesis. *Mon. Wea. Rev.,* **114,** 1340–1353.

Koshyk, J. N., and H.-R. Cho, 1992: Dynamics of a mature front in a uniform potential vorticity semigeostrophic model. *J. Atmos. Sci.,* **49,** 497–510.

Ley, B., and W. R. Peltier, 1978: Wave generation and frontal collapse. *J. Atmos. Sci.,* **35,** 3–17.

Lighthill, M. J., 1952: On sound generated aerodynamically. I. General theory. *Proc. Roy. Soc.* A, **211,** 564–587.

Lindzen, R. S., and M. Fox-Rabinovitz, 1989: Consistent vertical and horizontal resolution. *Mon. Wea. Rev.,* **117,** 2575–2583.

Lorenz, E. N., and V. Krishnamurty, 1987: On the nonexistence of a slow manifold. *J. Atmos. Sci.,* **44,** 2940–2950.

Nakamura, N., and I. M. Held, 1989: Nonlinear equilibration of two-dimensional Eady waves. *J. Atmos. Sci.,* **46,** 3055–3064.

Orlanski, I., and B. B. Ross, 1977: The circulation associated with a cold front. Part I: Dry case. *J. Atmos. Sci.,* **34,** 1619–1633.

——, and ——, 1984: The evolution of an observed cold front. Part II: Mesoscale dynamics. *J. Atmos. Sci.,* **41,** 1669–1703.

Pecnick, M. J., and D. Keyser, 1989: The effect of spatial resolution on the simulation of upper-tropospheric frontogenesis using a sigma-coordinate primitive equation model. *Meteor. Atmos. Phys.,* **40,** 137–149.

Persson, P. O. G., and T. T. Warner, 1991: Model generation of spurious gravity waves due to inconsistency of the vertical and horizontal resolution. *Mon. Wea. Rev.,* **119,** 917–935.

Polavarapu, S. M., and W. R. Peltier, 1990: The structure and nonlinear evolution of synoptic scale cyclones: Life cycle simulations with a cloud scale model. *J. Atmos. Sci.,* **47,** 2645–2672.

Reeder, M. J., and D. Keyser, 1988: Balanced and unbalanced upper-level frontogenesis. *J. Atmos. Sci.,* **45,** 3366–3386.

Robert, A. J., 1966: The integration of a low order spectral form of the primitive meteorological equations. *J. Meteor. Soc. Japan,* **44,** 237–245.

Sawyer, J. S., 1956: The vertical circulation at meteorological fronts and its relation to frontogenesis. *Proc. Roy. Soc. London,* A234, 346–362.

Skamarock, W. C., and J. B. Klemp, 1992: Adaptive grid refinement for 2D and 3D nonhydrostatic atmospheric flow. *Mon. Wea. Rev.,* **121,** 788–804.

Spall, M. A., and J. C. McWilliams, 1992: Rotational and gravitational influences on the degree of balance in the shallow-water equations. *Geophys. Astrophys. Fluid Dyn.,* **64,** 1–30.

Tremblay, A., 1992: Structure and development of mesoscale baroclinic waves in nonhydrostatic numerical model. *Mon. Wea. Rev.,* **120,** 463–481.

Volkert, H., and C. H. Bishop, 1990: The semi-geostrophic Eady problem as a testbed for numerical simulations of frontogenesis. *Tellus,* 42A, 202–207.

Williams, R. T., 1967: Atmospheric frontogenesis: A numerical experiment. *J. Atmos. Sci.,* **24,** 627–641.

——, 1972: Quasi-geostrophic versus nongeostrophic frontogenesis. *J. Atmos. Sci.,* **29,** 3–10.

——, 1974: Numerical simulation of steady-state fronts. *J. Atmos. Sci.,* **31,** 1286–1296.